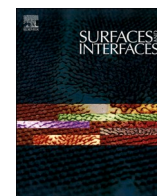| Title	NiTi coating formation on Ti for enhanced wear resistance utilizing electron-beam additive manufacturing technique
Author(s)	Wang, Lei; Okugawa, Masayuki; Liu, Yuheng et al.
Citation	Surfaces and Interfaces. 2025, 72, p. 107024
Version Type	VoR
URL	https://hdl.handle.net/11094/102624
rights	This article is licensed under a Creative Commons Attribution-NonCommercial 4.0 International License.
Note	

NiTi coating formation on Ti for enhanced wear resistance utilizing electron-beam additive manufacturing technique

Lei Wang [a], Masayuki Okugawa [a,b,*], Yuheng Liu [a], Ken Cho [a,b], Hiroyuki Y. Yasuda [a,b], Takayoshi Nakano [a,b], Yuichiro Koizumi [a,b,*]

[a] Graduate School of Engineering, The University of Osaka, 2-1 Yamadaoka, Suita, Osaka 565-0871, Japan
[b] Anisotropic Design & Additive Manufacturing Research Center, The University of Osaka, Suita 565-0871, Japan

ARTICLE INFO

ABSTRACT

Titanium and its alloys are extensively utilized in various industries owing to their high corrosion resistance and excellent strength-to-weight ratio. However, their poor wear resistance limits further applications. The present study developed a novel method to fabricate wear-resistant NiTi coatings on commercially pure titanium (CP-Ti) substrates to overcome this limitation. The process comprises electroplating a pure Ni layer followed by fusion with the CP-Ti substrate by electron beam (EB) scanning. The surface roughness and composition of the coating can be fine-tuned by adjusting the EB irradiation conditions. For example, the average roughness of continuously scanned (CS) coatings is Ra 8.9, while the average roughness of intermittently scanned (IS) coatings is reduced by 60 % compared to CS-coatings. Additionally, the Ni concentration in the IS-coatings can be finely adjusted from 45 at.% to 55 at.% by adjusting EB power. X-ray diffractometry (XRD) revealed that IS-coatings are partially composed of superelastic $B2$-NiTi phases. Nanoindentation and sliding wear tests demonstrated that the hardness-to-modulus (H/E) ratio and depth recovery ratio ($\eta_{d,h}$) of the IS-coating increased by a factor of 4.7 and 2.9 compared to those of CP-Ti, respectively. Additionally, the specific wear rate (W_s) of the IS-coating was reduced by 80 % compared to CP-Ti. The mechanical properties of the IS-coating were comparable to those of superelastic NiTi alloy. This newly developed method offers potential applications beyond NiTi coatings, enabling the development of various functional coatings for enhanced wear resistance.

1. Introduction

Commercially pure titanium (CP-Ti) has extensive applications in biomedical [1], aerospace [2], chemical [3], marine [4], and nuclear sectors [5] owing to its high corrosion resistance, biocompatibility, lightweight nature, and high specific strength [6]. However, the inferior wear resistance of CP-Ti limits its application in critical transmission components including engines and pumps [7,8]. Alloying can enhance wear resistance to a certain degree; however, it impacts the bulk properties. For example, Ti-6Al-4 V alloys show a wear rate under dry friction conditions that is approximately 50 % lower than that of CP-Ti [9,10]. However, this improvement is not adequate, as alloying compromises ductility. The tensile elongation of Ti-6Al-4 V is reduced to approximately 10 % [11], which is nearly half that of CP-Ti.

Surface engineering offers an effective way to improve surface properties, such as wear resistance, and gives a new function to the surface while maintaining the bulk properties [12–14]. Coating[15,16]

is a common method of surface treatment in the field of surface engineering. This method protects the substrate by covering it with another, more wear-resistant material. Among various coating materials, we specifically focus on NiTi alloy as it stands out as an excellent coating material[17–26].

NiTi alloys exhibit superelasticity (SE) [27,28], which can contribute to the enhancement of wear resistance, although it depends on the temperature and alloy composition. In fact, NiTi alloys possess wear resistance superior to that of Ti-6Al-4 V [29]. Utilizing NiTi alloy coatings could effectively mitigate the wear resistance deficiencies of CP-Ti. Additionally, the shape memory effect (SME) inherent in NiTi offers the potential to create self-healing surfaces upon exposure to heat [30,31]. NiTi coatings have been deposited using conventional coating methods such as laser plasma spraying [19,20], vacuum plasma spraying [21,22], atmospheric plasma spraying [23], cold spraying [24–26], and magnetron sputtering [17,18]. However, NiTi alloy coatings produced by spraying tend to exhibit microstructural nonuniformities, with

variations in compositions and phases across spatial scales of tens of micrometers [20]. These coatings also contain unfused regions and oxide formations [22,23]. Eliminating these defects is crucial for the development of coatings with enhanced SME and SE. Although magnetron-sputtered coatings exhibit a fine and homogeneous microstructure, their limited thickness hinders their effectiveness in wear-resistant applications [17,18].

Electroplating is a simple and low-cost coating technique [32], capable of producing uniform and dense layers [33,34]. It is considered a suitable method for addressing defects commonly found in thermal spray coatings. However, the direct formation of intermetallic compounds in NiTi alloys via electroplating remains challenging. In recent years, a new manufacturing approach has emerged: the fabrication of layered structures using additive manufacturing (AM). This method enables the use of low-cost, conventional materials for the substrate while applying high-performance materials with superior wear and corrosion resistance as the surface layer, thereby enhancing surface properties [35–37]. Inspired by the above studies, a novel approach combining electroplating with AM (specifically, electron beam melting, EBM) was proposed to fabricate NiTi coatings in our previous study [38]. The NiTi coatings are synthesized in two steps: 1. electroplating a pure Ni layer on CP-Ti; 2. irradiating with an electron beam (EB). This method integrates the simplicity and cost-effectiveness of electroplating with the flexibility and controllability of AM.

Single-track experiments were performed to examine the feasibility of this method for forming NiTi alloy coatings in the previous study [38]. A NiTi alloy layer with a nearly stoichiometric composition was successfully obtained by optimizing the EB irradiation conditions. However, a single-track NiTi layer cannot be directly used as a practical coating. Only by arranging multiple tracks in parallel and close to each other to completely cover the material surface can NiTi coatings with practical applications be produced [38,39]. Moreover, the multi-track scanning process is not simply a repetition of single-track scanning; the interactions between neighboring tracks must be considered. Therefore, the EB irradiation conditions used in single-track scanning cannot be directly applied to the multi-track scanning process, which requires dedicated study and optimization. This then becomes the main objective of the present study.

In the present study, NiTi alloy coatings were fabricated by multitrack EB scanning of Ni-plated CP-Ti substrates under various EB irradiation conditions. The relationship between the process conditions and the quality of coatings, including compositional homogeneity, constituent phases, and mechanical properties, was investigated from the perspective of melting, mixing, solidification, and solid-state diffusion. Furthermore, the novel NiTi coating approach integrated electroplating and AM techniques, offering useful insights for surface engineering. Such integration takes advantage of the reliability and cost-effectiveness of conventional techniques, along with the precision and adaptability of modern approaches.

2. Methods

2.1. Preparation of substrate and Ni-plate

A slab of CP-Ti (99.5% purity; Nilaco, Tokyo, Japan) was cut into specimens of $25 \times 25 \times 10$ mm^3 by electric discharge machining. A CP-Ti specimen of 25×25 mm^2 area was used as the working electrode. The CP-Ti specimen was given a four-stage pretreatment: (1) mechanical grinding using P120–P2400-grit SiC abrasive papers; (2) immersion in ethanol at RT for 5 min; (3) immersion 10 wt.% HCl solution at RT for 5 min, with a 9 V DC power applied to promote the removal of surface oxides and contaminants, and (4) washing with ultrapure water.

A Pure Ni anode ($\Phi6 \times 20$ mm) of 405 mm^2 area was used with an interelectrode gap of 8 cm. In this study, a thicker pure Ni layer was required to enable subsequent processing. Therefore, a nickel sulfamate solution was used as the plating bath. This type of bath tolerates high

current density and produces plated layers with lower internal stress, making it suitable for applications that demand greater coating thickness [40]. The compositions of the solutions and the electroplating parameters adopted from an electrochemical handbook [40] are listed in Table 1. Electroplating was conducted for 4 h to obtain a plating layer with sufficient thickness. After plating, the layer was ground using P120–P2000 grit SiC abrasive papers to a final thickness of 45 μm.

2.2. Electron beam irradiation

The plated specimens were irradiated with EBs using an EBM machine (EBM-6LB-1, Mitsubishi Electric) in a helium atmosphere at 0.5 Pa. Multi-track scanning was performed over a 3×4 mm^2 area using a serpentine scanning process (Fig. 1). The electron beam power (P) was set at four levels of 126, 132, 138, and 144 W. The line offset and scanning speed were fixed at 300 μm and 100 mm/s, respectively. The multi-track scanning experiments were conducted using two scanning modes—continuous scanning and intermittent scanning — to regulate the thermal effect induced by the preceding scanning. Continuous scanning mode had no intervals between consecutive track scans ($t_{int} = 0$ s), whereas intermittent scanning mode included a 60-s interval between scans ($t_{int} = 60$ s). In the intermittent scanning mode, the specimens were cooled before the subsequent beam scan. Although the interval of 60 s might be too long for an actual process, it was employed to perform experiments under near-ideal conditions with sufficient cooling time.

2.3. Microstructural characterization

The top surfaces of the multi-scanned specimens were observed using a confocal laser scanning microscope (VK-X200/210, Keyence, Japan). The samples were then cut perpendicular to the beam-scanning direction for cross-sectional observation by field-emission scanning electron microscopy (FE-SEM; JSM 6500, JEOL, Japan). The elemental distributions were analyzed by energy-dispersive X-ray spectroscopy (EDS). X-ray diffractometry (XRD; SmartLab SE diffractometer, Rigaku, Japan) identified the crystallographic phases of the surface layer. In the XRD tests, the ray source was Cu Kα and the 2theta scanning range was 20°–80° with a step size of 0.01°. The test for each sample was conducted 3 times in the same condition. The formed Ni-Ti alloy phases were studied by evaluating the equilibrium phase characteristics of the Ni-Ti binary alloy using Thermo-Calc Software (version 2022b) with a thermodynamic database for Ti alloys (TCTI4) [41].

2.4. Nanoindentation tests

Nanoindentation tests were performed using a nanoindentation tester (ENT-1100a, Elionix, Japan) equipped with a Berkovich indenter to evaluate the indentation properties of the EB-scanned coating. Before the tests, the surfaces of specimens were ground using P120–P4000-grit SiC abrasive papers and then polished using 50 nm alkaline colloidal silica suspension. The Nanoindentation tests were performed at 26 °C inside the device equipped with a shield case to prevent thermal drift. A total of 50 equally spaced points were selected on each sample to repeat the test under identical parameters. Then, the results were averaged to

Table 1
Composition of Ni-plating solution and plating parameters.

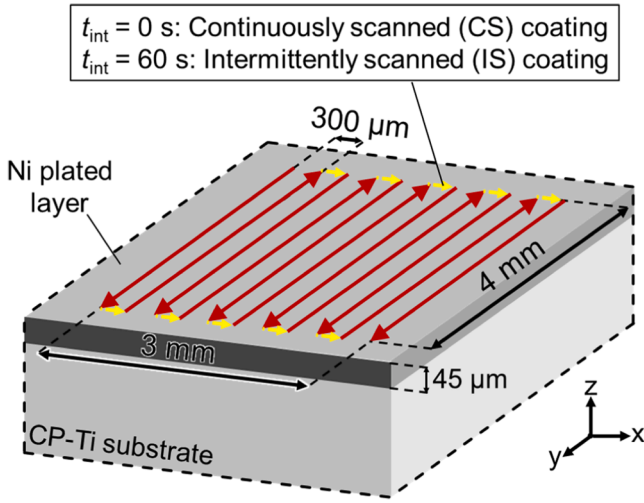|	Compound/Parameter	Value
Composition	NiCl$_2$·6H$_2$O	0.10–0.13 mol/L
	Ni(SO$_3$NH$_2$)$_2$	1.70–1.79 mol/L
	H$_3$BO$_3$	0.49–0.73 mol/L
Parameters	Temperature	50–60 °C
	pH	3.0–5.0
	Cathodic current density	3.0 A/dm^2
	Current mode	DC plating

Fig. 1. Schematic of a Ni-plated CP-Ti substrate subjected to EB scanning.

eliminate the effect of randomness. The peak load was 50 mN, and the loading rate was 5 mN/s. The Berkovich indenter [42] with an apex angle of 65.03° was used, and the following relationship between the indenter contact area (A) and indentation depth (h) was employed:

$$A = 3\sqrt{3}\tan^2(65.03°)\cdot(h + \Delta h)^2. \tag{1}$$

Here, Δh is the indenter tip correction value calculated using the Sawa–Tanaka method [43] based on the indentation results of a standard fused silica sample. From the obtained results, Young's modulus (E) and hardness (H) were calculated according to the ISO 14,577–1 protocol [44]. Moreover, depth recovery ratio ($\eta_{d,h}$) is defined as the ratio of recoverable indentation depth to indenter displacement at maximum load [45]. It was calculated as follows:

$$\eta_{d,h} = \frac{h_{\max} - h_p}{h_{\max}}, \tag{2}$$

where $h_{\max}$ and h_p are the maximum penetration depth of the indenter during the indentation tests and the permanent depth after load removal, respectively.

2.5. Sliding wear tests

Sliding wear tests were conducted according to the ASTM G133–22 standard [46] on an oscillation sliding tester (OST3000, Rhesca, Japan) to evaluate the wear resistance of the intermittently scanned (IS) coating. Before the tests, the surfaces of specimens were ground using P120–P4000-grit SiC abrasive papers and then polished using 50 nm alkaline colloidal silica suspension. The tests were conducted under a constant load (L) of 50 N using an alumina ceramic indenter. The diameter of the indenter is 9.5 mm and the hardness is 2085 HV$_{0.1}$ [47]. The specimens were subjected to a 1 Hz oscillation with an 8 mm amplitude. The test duration for each specimen was 625 s, resulting in a total sliding distance (D) of 10 m (= 8 mm × 2 × 625 s). The temperature inside the tester during the test was maintained at 26 °C and the relative humidity was maintained at 50%. The same wear test was conducted 2 times on each specimen. The friction coefficient (μ) was evaluated as follows:

$$\mu = \frac{F_Z}{F_T}, \tag{3}$$

where F_Z and F_T are normal and tangential loads, respectively. Both were measured and continuously recorded by the integrated sensor during the tests.

Specific wear rate (W_s) is an indicator of the wear resistance of a material [48]. The W_s of specimens was evaluated as follows:

$$W_s = \frac{V}{LD}, \tag{4}$$

where V, L, and D are volume loss, applied load, and sliding distance, respectively. V was measured by the confocal laser scanning microscope after the sliding test. The worn surfaces were also observed using SEM and EDS. A commercially available superelastic NiTi alloy (Ni 50.6 at.%, Ti 49.4 at.%; Seemine Keli, Lanzhou, China) as well as the substrate, CP-Ti, were also tested as control specimens.

3. Results and discussion

3.1. Surface morphology and roughness

Fig. 2 shows surface morphology optical images and height maps obtained from the coatings formed by multi-track EB scanning under various conditions. The scanning direction of each track is parallel to the *y*-axis while the tracks fill the area along the *x*-axis in the positive direction.

In Figs. 2a–d, all height maps of continuous scanned (CS) coatings ($t_{int} = 0$ s) show sunken regions at the center of each coating. Protruding regions appeared at the right side of the CS-coatings at 132 and 144 W (Figs. 2b2 and d2). These protrusions can be attributed to the rapid heating of the substrate caused by the continuous scanning of the EB. The thermal stress generated by the large temperature gradient caused warping deformation of the Ni layer near the melt track and debonding with the substrate. Then, the liquid metal in the melt pool flows into the crevices under the debonded Ni-plating layer, forming a protruding surface after solidification. In Figs. 2e–h, the height maps of the intermittently scanned (IS) coatings ($t_{int} = 60$ s) show remarkably flat surfaces, without significant protrusion and sinkage. Notably, corrugated patterns are observed on the surfaces of the IS-coating (Figs. 2f2 and h2), whose patterns are similar to those of the single-track melt formed by EB irradiation in our previous study [38]. Cracks were generated perpendicular to the melt tracks on most CS-coatings (white triangles in Figs. 2a–d), while cracks did not appear on the IS-coatings. These cracks are presumably generated by residual stresses induced by the EB irradiation, as suggested by Li et al. [49] and Takase et al. [50], who reported that residual stresses up to hundreds of MPa could be generated in Ti alloys by EB-irradiation-induced melting and solidification in AM.

Fig. 3 shows the variation in the surface roughness of the coatings with P. The CS-coatings have significantly rougher surfaces and have more significant fluctuation in roughness than those of the IS-coatings. Among the experimental conditions, the IS-coating at 126 W has the lowest surface roughness ($R_a = 3.36$ μm), i.e., the smoothest surface.

The significant difference in surface topography and roughness between CS- and IS-coatings originates from the distinct melting and solidification processes in continuous and intermittent scanning modes. In continuous scanning (CS) mode, the electron beam scans adjacent tracks sequentially in a serpentine pattern. Track #n + 1 begins immediately after track #n, causing the melt pools to merge into a larger liquid zone. This larger melt pool leads to stronger liquid flow and steeper temperature gradients, resulting in pronounced macroscopic bumps and depressions after solidification. Consequently, CS-coated surfaces exhibit frequent surface undulations and high, fluctuating roughness values as electron beam power changes. In contrast, intermittent scanning (IS) mode introduces sufficient cooling time after each track, allowing the material to return nearly to room temperature and minimizing heat transfer to subsequent tracks. The melt pool remains localized within the current scanning area, leading to weaker fluid flow, smaller temperature gradients, and more uniform surface solidification. As a result, IS coatings are flatter, with consistently low roughness across different electron beam powers.
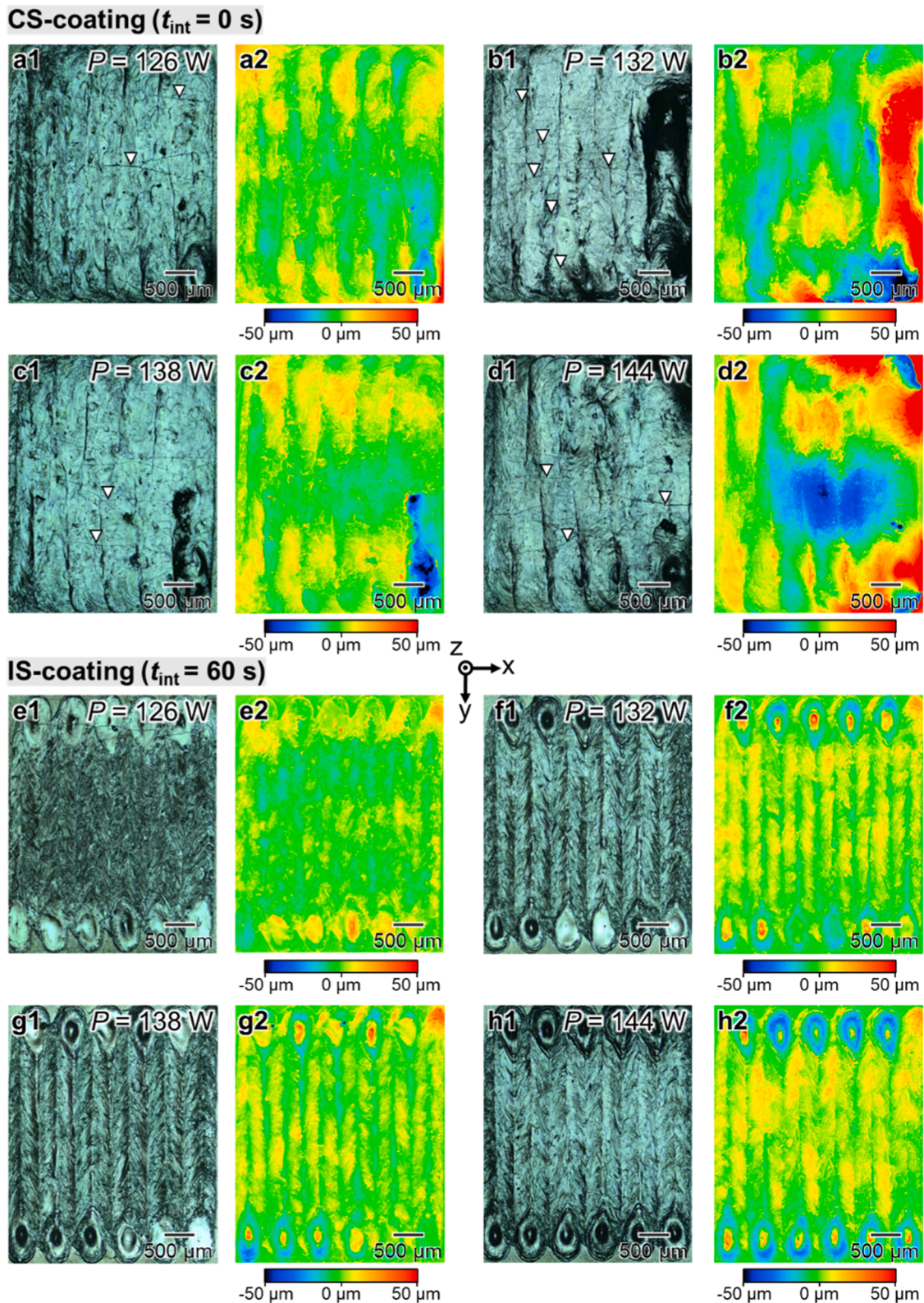
Fig. 2. Optical images and height maps of coatings fabricated by multi-track EB scanning under various conditions with: time intervals (t_{int}) of 0 s (a, b, c, d) and 60 s (e, f, g, h); EB power (P) of 126 W (a, e), 132 W (b, f), 138 W (c, g), and 144 W (d, h); scanning speed of 100 mm/s. The white triangles show the location of the cracks. "CS-coating" and "IS-coating" refer to continuously and intermittently scanned coatings, respectively.

3.2. Cross-sectional morphology of the melt region and elemental composition distribution

Fig. 4 shows the cross-sectional backscattered electron (BSE) images (Figs. 4a1, a2, b1, and b2) and the corresponding elemental distributions analyzed by SEM-EDS (Figs. 4a3 and b3) of EB-scanned coatings with processed data (Figs. 4c, d and e) from BSE images and EDS mapping images. The BSE images show regions with dark and bright contrasts.
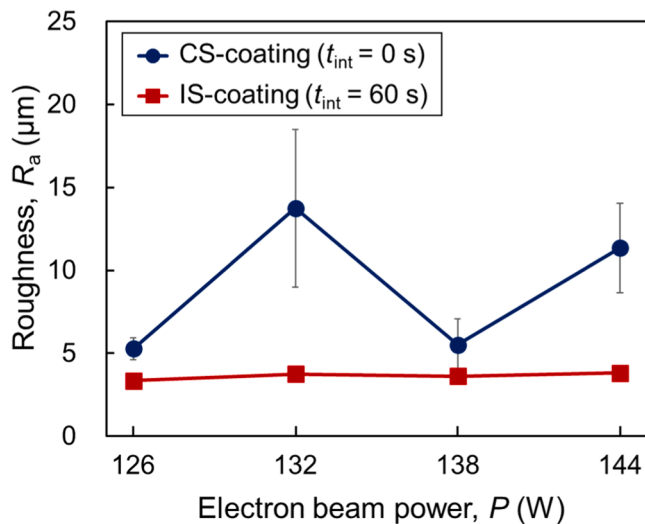
Fig. 3. Surface roughness (R_a) of EB-scanned coating fabricated under various scanning conditions as a function of EB power (P) with a constant scanning speed of 100 mm/s.

The dark regions at the bottom correspond to the CP-Ti substrate. The bright areas at the center of the images represent the coatings formed by multi-track scanning. The scanning sequence is from left to right. Unmelted Ni plates can be seen at the left edges where the surface was not irradiated with EB. Ni and Ti are mixed in the coatings formed by EB irradiation under both conditions presumably due to convection and diffusion in the liquid metals. Marangoni convection is considered to have played a crucial role in the mixing of pure Ni and Ti as indicated by the marble pattern. The Marangoni effect can significantly influence melting and solidification during EB irradiation because of the steep temperature gradient along the melt pool surface, which can be as high as 10^7 K/m. This gradient arises from localized heating by the EB, which has a diameter of approximately 100 μm [51].

The influence of process parameters on the cross-sectional morphology of the melt region and coating composition was then analyzed. For this, the Ti-melt depth (d_{Ti}) and Ni concentration (C_{Ni}) were quantified for each melt track. d_{Ti} represents the melt penetration depth into the CP-Ti substrate, defined as the vertical distance between the Ni-plate/Ti-substrate interface and the melt-track bottom (Figs. 4a2 and b2). C_{Ni} values were determined using EDS analysis of the melt-track regions in the elemental mapping images (Figs. 4a3 and b3).

Figs. 4c and d summarize the d_{Ti} and C_{Ni} data of the EB-scanned coatings under all scanning conditions. Fig. 4c shows the variation in d_{Ti} while Fig. 4d shows the variation in C_{Ni} with track number. Regardless of P, the d_{Ti} of continuously scanned (CS) coatings increases significantly with the number of melt tracks, showing an average rise of 60 μm from Track #1 to #11. As observed in laser powder bed fusion processes, continuous scanning is expected to cause heat accumulation [52]. A similar effect likely occurred in this study, leading to the increase in d_{Ti}. The growth in d_{Ti} is rapid from Track #1 to #4; however, it gradually stabilizes after Track #4, although the overall trend remains upward. In contrast, the d_{Ti} of intermittently scanned (IS) coatings remains relatively stable, fluctuating only slightly within a range of approximately 15 μm from Track #1 to #11. The C_{Ni} of CS-coatings is negatively correlated to d_{Ti}, gradually decreasing from Track #1 to #11 by an average of 13 at.%. This trend is consistent with predictions based on mass conservation. Specifically, the Ni in the melt track originates from Ni plating, and as the thickness of the Ni plating is uniform, the amount of Ni in the melt track remains constant. Conversely, Ti in the melt track is supplied from the Ti substrate. As d_{Ti} increases, a larger amount of Ti enters the melt track, causing a relative decrease in C_{Ni}, as evidenced in the data. This indicates that the

composition of the melt track changes as the scanning progresses during continuous scanning, leading to variations in the mechanical properties of the formed coating. Hence, the CS-coating becomes inhomogeneous among melt tracks, rendering controlling its properties through adjustments to the scanning parameters challenging. Conversely, C_{Ni} of IS-coatings exhibits a minor decreasing trend from Track #1 to #3. From Track #4, C_{Ni} stabilizes and fluctuates within a range of approximately 1 at.%. The EB-induced temperature accumulation is considered to have decreased during the 60-s interval. This suggests that the melting and solidification behaviors in all tracks of IS-coatings are essentially the same as those in single-track scanning. Therefore, IS-coatings demonstrate a stable composition and structure across all tracks, facilitating more precise control over the coating composition and properties.

Fig. 4e summarizes the average values of d_{Ti} and C_{Ni} across all melt tracks of every EB-scanned coating, showing the variation in the structure and composition of coatings in general. C_{Ni} decreases monotonically with increasing d_{Ti} in both CS- and IS-coatings. Generally, d_{Ti} is higher in CS-coatings than in IS-coatings. Conversely, C_{Ni} is lower in CS-coatings than in IS-coatings, which is closer to the target value of 50 at. %, i.e., the stoichiometric composition of the NiTi phase. The C_{Ni} of the IS-coating scanned at 126 W is higher than 50 at.%, approximately 50 at. % at 132 W, and lower than 50 at.% at 138 and 144 W. Fig. 4f shows the equilibrium phase diagram of the Ni-Ti binary system. At temperatures around 1400 K, the NiTi monophase can be stable at 49.3–56.7 at.% Ni concentration. However, when the temperature is lowered to 400 K, the NiTi monophase can occur predominantly at Ni concentration equal to 50 at.%. This means that a slight deviation in Ni concentration from 50 at.% in NiTi alloys may lead to phase separation during the equilibrium solidification process. However, the melt pool undergoes non-equilibrium solidification due to the steep temperature gradient and rapid solidification rate during the EB scanning process, reaching up to 10^7 K/m and 10 m/s, respectively [51]. Therefore, the rapid solidification process enables higher Ni or Ti concentrations in the NiTi phase compared to the equilibrium state, preventing phase separation [53]. This indicates that IS-coatings contain a higher amount of the NiTi primary phase and a lower amount of secondary phases (NiTi$_2$ and Ni$_3$Ti) compared to cast Ni-Ti alloy with the same composition. In contrast, the C_{Ni} in CS-coatings is 8 at.% lower than 50 at.% or less, inevitably leading to the formation of a significant amount of NiTi$_2$ phase.

Fig. 5 shows the cross-sectional morphology (BSE images) and corresponding elemental composition distribution (EDS maps) from Tracks #6 to #7 of coatings fabricated by multi-track EB scanning under various conditions. In general, the brightness of BSE images is associated with the atomic mass of the elements present in the observed material. Specifically, higher atomic masses result in brighter images. In this study, a higher content of the element nickel (Ni) shows a higher brightness. The BSE images (Figs. 5a1, b1, c1, and d1) of the CS-coatings show noticeable variations in brightness across different regions. This suggests that the coatings experienced micrometer-scale segregation during the solidification process, resulting in an uneven distribution of elements. This observation is supported by the corresponding EDS mapping (Figs. 5a3, b3, c3, and d3). The magnified BSE images of the CS-coatings (Figs. 5a2, b2, c2, and d2) show that the microstructure evolves with increasing electron beam power (P). Phase identification was supported by the corresponding EDS mappings (Figs. 5a4, b4, c4, and d4). At 126 W, the microstructure consists of NiTi dendrites with NiTi$_2$ phases distributed between them. At 132 W, 138 W, and 144 W, the matrix is predominantly composed of NiTi$_2$, with a small amount of NiTi dendrites remaining in localized areas. In addition, a darker phase appears between NiTi$_2$ dendrites in regions with significantly lower Ni concentration. Detailed examination of EDS data reveals that the Ni concentration in these regions is close to 25 at.%, which marks the (βTi+Ti$_2$Ni) eutectic point in the Ni-Ti binary system (Fig. 4f). Additionally, cracks are visible in the cross-section of the CS-coatings, as indicated by the red arrows, which aligns with the findings from the
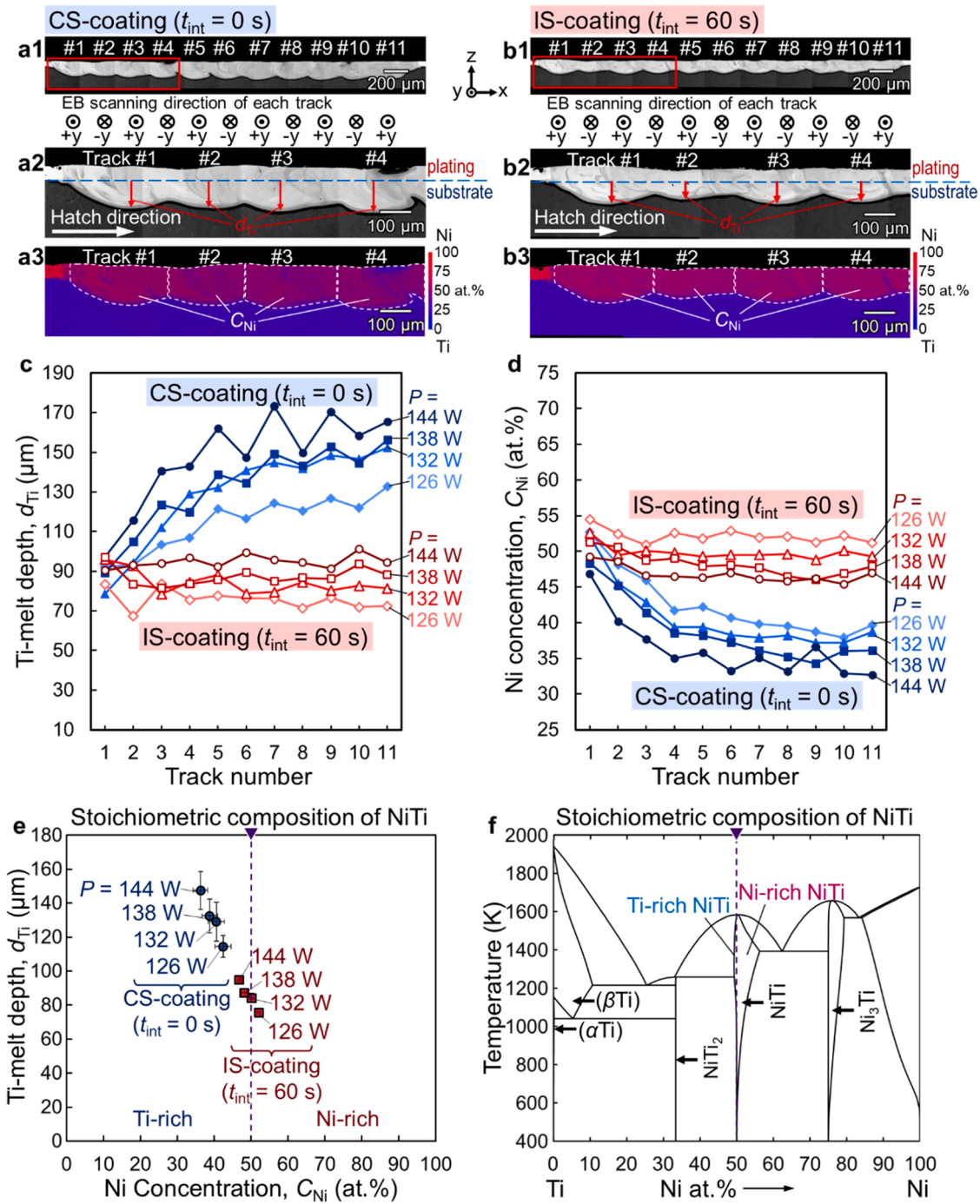
Fig. 4. Cross-sectional BSE images (a1, a2, b1, b2) and corresponding EDS mapping (a3, b3) of melt tracks in (a) continuously scanned (CS) coating: $t_{int} = 0$ s, $P = 126$ W; (b) intermittently scanned (IS) coating: $t_{int} = 60$ s, $P = 126$ W. (c) Variation in Ti-melt depth (d_{Ti}) with the track number in EB-scanned coatings. (d) Variation in the Ni concentration (C_{Ni}) with the track number in EB-scanned coatings. (e) Plot of d_{Ti} versus C_{Ni} in the EB-scanned coating with various scanning conditions. (f) Ni-Ti binary equilibrium phase diagram.

surface observation (Fig. 2). These cracks primarily appear in the (βTi+Ti$_2$Ni) eutectic areas according to BSE images in Fig. 5.

The BSE images (Figs. 5e1, f1, g1, and h1) of the IS-coatings show that the IS-coatings under all four levels of P have more uniform brightness distributions than the CS-coatings. This suggests that the elemental distributions are also more homogeneous in the IS-coatings. However, some dark streaks can be seen at the junction of the melt tracks as indicated by black arrows. These dark streaks are less frequent and narrower at 126 and 132 W. Conversely, they are wider and more frequent at the junction region between every two tracks at 138 and 144

W. Additionally, EDS mappings (Figs. 5e3, f3, g3, and h3) show lower Ni concentration (~33 at.%) in the regions corresponding to these dark streaks compared to the average composition of the coating. The magnified BSE images of the IS coatings (Figs. 5e3, f3, g3, and h3) reveal significant changes in microstructure with increasing electron beam power. Phase identification is supported by the corresponding EDS mappings (Figs. 5e4, f4, g4, and h4). At 126 W and 132 W, the coating matrix exhibits a cellular NiTi structure, with dark streaks—<1 µm wide—identified as NiTi$_2$ phase. When the power increases to 138 W, the cellular structure disappears. In this case, the dark regions consist of
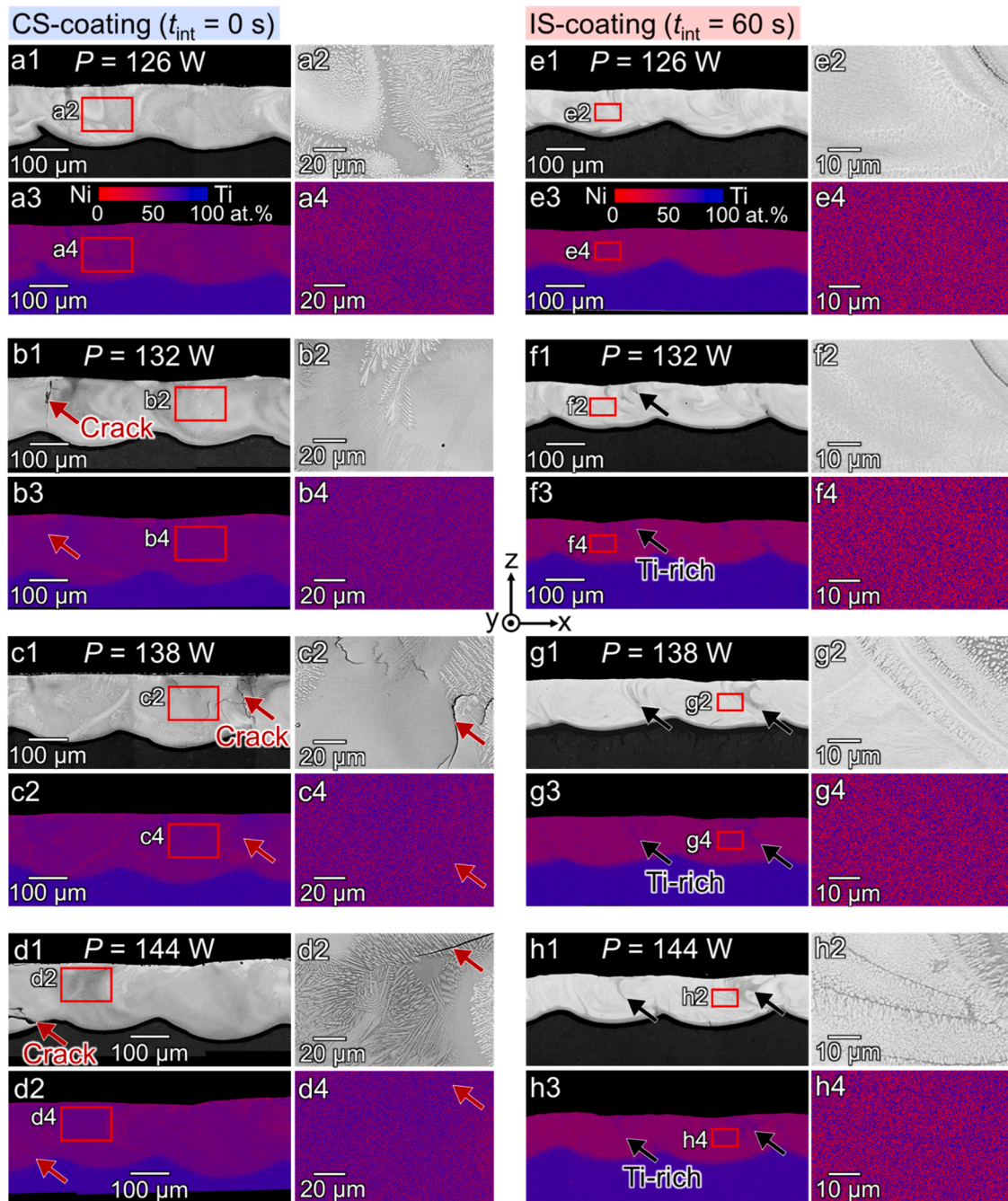
Fig. 5. (*a* − *h*) BSE images and EDS mapping of the cross-section of Track #6 to #7 in all EB-scanned coatings for the CS-coatings (left) and IS-coatings (right). *P* of (a, e) 126 W, (b, f) 132 W, (c, g) 138 W and (d, h) 144 W. Red arrows indicate cracks while black arrows indicate Ti-rich regions in BSE images.

NiTi dendrites with $NiTi_2$ phase filling the spaces between them. At 144 W, both the matrix and the dark regions contain NiTi dendrites and inter-dendritic $NiTi_2$, but the dendrites in the dark regions are more widely spaced. These observations suggest that IS-coatings fabricated at 126 W and 132 W, which retain a cellular structure and have a lower $NiTi_2$ content, are expected to exhibit superior mechanical properties compared to those fabricated at 138 W and 144 W, as well as all CS-coatings.

Notably, cracks appear near these dark regions with relatively low Ni concentration (Ti-rich) in the CS-coatings exclusively. This observation is proposed to be attributed to liquation cracking owing to the lower melting temperature of the Ti-rich regions. Furthermore, heat accumulation during the continuous scanning process will promote cracking. According to the Ni-Ti phase diagram (Fig. 4f), the composition of the

Ti-rich region corresponds to the lower liquid-phase temperature. This indicates that most of the coating had already solidified and begun to cool and contract when the Ti-rich region started to solidify, leading to tensile stress concentration in the Ti-rich regions and increasing the probability of cracking [54]. Conversely, the absence of cracks in the IS-coatings can be attributed to two factors. First, intermittently scanning prevents excessive heat buildup, lowering the maximum melt-pool temperature and reducing thermal stresses. Second, the Ti-rich regions (dark contrast region) in the IS-coatings are significantly smaller.

3.3. Phase identification

Fig. 6 shows the XRD profiles of the EB-scanned coating and the variation in intensity of selected characteristic peaks with *P* in

Fig. 6. X-ray diffraction (XRD) patterns of the EB-scanned coatings. (a) Results for the continuously scanned (CS) coatings with the as-plated specimen as control. (b) Results for the intermittently scanned (IS) coatings. Variation in intensity of (c) $B2$-NiTi (110) peak, (d) NiTi$_2$ (511) peak, and (e) Ni$_3$Ti (20$\overline{2}$1) peak with EB power in CS- and IS-coatings.

continuously scanned (CS) and intermittently scanned (IS) coatings. The positions of the characteristic peaks were compared with 6 PDF cards to identify the phases: #00–001–1260 (Ni), #01–076–3614 ($B2$-NiTi), #01–078–4618 ($B2$-NiTi), #01–072–8488 ($B19$'-NiTi), #01–075–0878 (Ni$_3$Ti), #00–005–0687 (NiTi$_2$). Data from other studies [55–57] were also referenced to assist in phase identification. The five profiles in Fig. 6a, from top to bottom, represent the as-deposited Ni plating (control) and the CS-coating with P of 126, 132, 138, and 144 W, respectively. Only the characteristic peaks of NiTi$_2$ and NiTi phases are observed on the profiles of all coatings. Owing to the low C_{Ni} in CS-coatings, the intensity of the NiTi$_2$ characteristic peaks is significantly higher than that of the NiTi peaks across all profiles. The variation in intensity of $B2$-NiTi (110) and NiTi$_2$ (511) (Figs. 6c and d) indicates that the small amount of $B2$-NiTi phase in the CS-coatings decreases further with increasing P. The $B2$-NiTi phase nearly disappears at 144 W, leaving NiTi$_2$ as the dominant phase in the coatings. This observation is consistent with the cross-sectional BSE images (Fig. 5) discussed in *Section 3.2*.
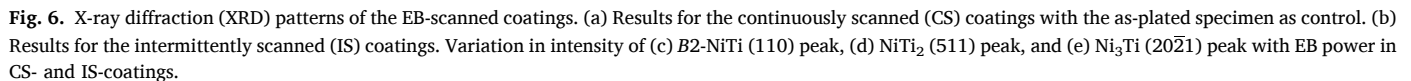
Fig. 6b shows the profiles of the IS-coatings with P of 126, 132, 138, and 144 W. Similar to the profiles in Fig. 6a, no characteristic peaks of Ni or Ti phases are observed in any of the coating profiles. This indicates that EB scanning fully mixes the Ni plating and CP-Ti substrate to form an alloy phase, regardless of the scanning parameters. Examining the four profiles of the IS-coatings alongside the variation in the $B2$-NiTi (110), NiTi$_2$ (511), and NiTi$_3$ (20$\overline{2}$1) peaks (Figs. 6c, d, and e) reveals that the $B2$-NiTi phase is predominant in all four coatings and reaches its highest concentration at 132 W. As P increases, the NiTi$_2$ phase, which is absent at 126 W, first appears at 132 W and then grows rapidly. Meanwhile, the NiTi$_3$ phase, present at 126 W, decreases and eventually disappears as P increases beyond 138 W. These variations in the phase

content within the coating essentially align with the trends in the binary Ni-Ti phase diagram (Fig. 4f).

The $B2$-NiTi phase is the primary phase in superelastic NiTi alloys, contributing to the superelastic properties [58]. In addition, Ni$_3$Ti exhibits the highest hardness and mechanical strength among all Ni-Ti intermetallic compounds [59] and is typically considered a strengthening phase in NiTi alloys. In contrast, NiTi$_2$ has relatively low hardness and strength and is prone to brittle fracture [60]. Owing to the heat accumulation effect, the C_{Ni} of the CS-coatings is significantly lower than that of the IS-coatings, even though both are scanned at $P = 126$ W. Therefore, as shown by the comparison of the intensities of the $B2$-NiTi (110) and NiTi$_2$ (511) peaks between CS- and IS-coatings, CS-coatings are mainly composed of the NiTi$_2$ phase, whereas IS-coatings have a superior structure with $B2$-NiTi as the primary phase and Ni$_3$Ti as the reinforcing phase. Thus, IS-coatings could be inferred to have better toughness, mechanical strength, and wear resistance than CS-coatings.

3.4. Indentation properties

3.4.1. Nanoindentation test results

Fig. 7a shows the load–displacement curves from the indentation tests of EB-scanned coatings, commercially available NiTi alloy (superelastic), and CP-Ti. Overlapping curves were avoided by presenting only the data for continuously scanned (CS) and intermittently scanned (IS) coatings produced at 126 W. The maximum indenter penetration depth during loading (h_{max}) and the permanent indentation depth after unloading (h_p) can be intuitively inferred from these curves. Fig. 7b shows the hardness (H) versus depth recovery ratio ($\eta_{d,h}$) plot of EB-scanned coatings. $\eta_{d,h}$ is defined as the ratio of the recoverable indentation depth to the maximum indentation depth, as given by Eq.
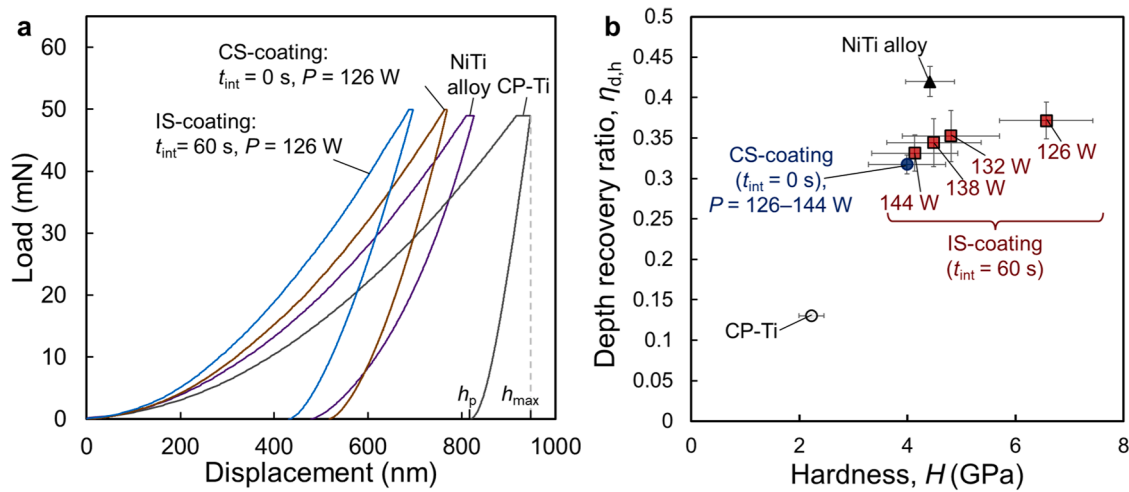
Fig. 7. (a) Load–displacement curve of Berkovich indentation tests on CP-Ti, NiTi alloy, and EB-scanned coatings. (b) Depth recovery ratio ($\eta_{d,h}$) vs. hardness (H) plot of CP-Ti, NiTi alloy, and EB-scanned coatings. "CS-coating" and "IS-coating" refer to continuously and intermittently scanned coatings, respectively.

(2). This index characterizes the elastic recovery properties of the material and has been shown to positively correlate with wear resistance in materials such as nanocomposites [61] and Ni-Ti alloys [57,62]. For the CS-coating, both H and $\eta_{d,h}$ are generally lower and display minimal variation as P changes. Consequently, the results obtained from all four levels of P can be represented by a single data point in the figure. Conversely, the IS-coatings exhibit a gradual increase in H and $\eta_{d,h}$ as P decreases, such that the coating produced at 126 W achieves the highest H and $\eta_{d,h}$ among all coatings. This trend may be attributed to the increasing fractions of Ni_3Ti and $B2$–NiTi phases and a decreasing fraction of $NiTi_2$ (Fig. 6). All EB-scanned coatings show considerably higher H and $\eta_{d,h}$ than CP-Ti. The IS-coatings exhibit higher H and $\eta_{d,h}$ than the CS-coatings.

Fig. 8a shows the variation of H and E in EB-scanned coatings with respect to P. For CS-coatings, H is lower than that of NiTi alloys and remains nearly constant regardless of P. In contrast, for IS-coatings, H increases as P decreases and exceeds that of the NiTi alloy when $P < 138$ W. A similar trend is observed for E: it remains stable for CS-coatings but increases with decreasing P for IS-coatings. Notably, E is higher for IS-coatings compared to CS-coatings at all P values; it is slightly above NiTi alloys but well below CP-Ti. Fig. 8b shows the hardness-to-modulus ratio (H/E) of all EB-scanned coatings. The H/E ratios of all EB-scanned coatings are significantly higher than CP-Ti. CS-coatings exhibit H/E ratios of approximately 0.06, regardless of P. In contrast, H/E for IS-

coatings increases as P decreases, surpassing CS-coating at $P = 126$ and 132 W. Although the H/E ratios of most coatings are slightly lower than those of NiTi alloys, the IS-coating at 126 W matches or even exceeds them. Higher hardness generally indicates improved wear resistance [63]; however, several recent studies [64–66] have suggested that the H/E ratio is a more reliable indicator, as it better correlates with wear resistance indicator than hardness alone. Therefore, a higher H/E ratio of EB-scanned coatings indicates that the coating could significantly improve the wear resistance of CP-Ti substrates.

3.4.2. Comparative analysis of indentation properties in EB-scanned coatings

Figs. 9a and b compare the parameters H/E ratio, H, and E of EB-scanned coatings with other materials such as structural metal (SM), superelastic NiTi alloy (SE-NiTi), wear-resistant (WR) coating, and NiTi alloy coating from other studies. Commonly used SMs have hardness in the range 1–10 GPa and Young's moduli of approximately 100–300 GPa. WR-coatings are typically used for surface protection of SMs, and their hardness and H/E ratios are higher than those of most SMs. Although SE-NiTi does not exhibit a hardness higher than SM or WR-coating, its lower Young's modulus gives it a considerably higher H and H/E ratio than that of SM or WR-coating. The EB-scanned coatings in this study have H and E values similar to those of SE-NiTi, resulting in improved H/E ratios compared to those of SM and WR-coatings. In particular, the IS-coating
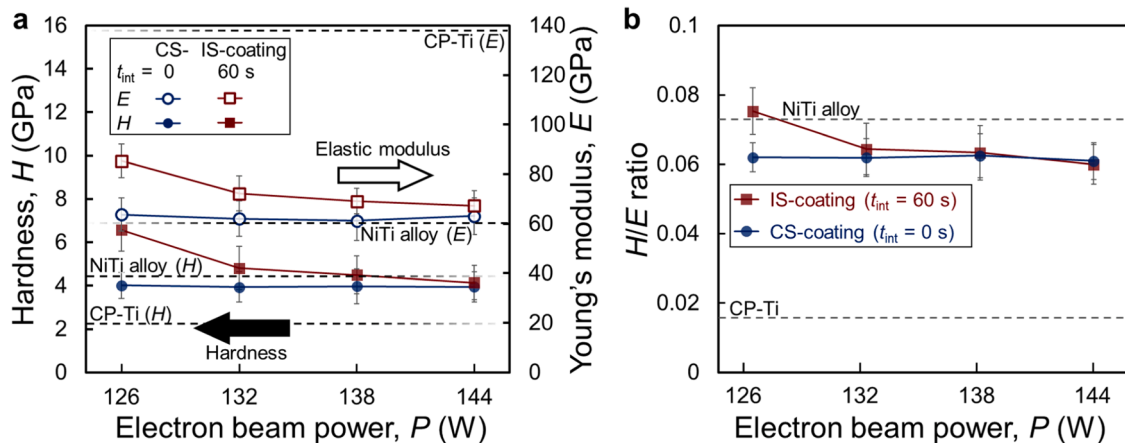
Fig. 8. (a) Variation in hardness (H) and Young's modulus (E) of coatings with increasing EB power (P). The solid points in the graph represent hardness (left vertical axis), while the hollow points represent Young's modulus (right vertical axis). The dashed lines represent the H and E of the reference NiTi alloy and CP-Ti. (b) Variation in H/E ratio of coatings with increasing P. The dashed lines represent the H/E ratio of the reference NiTi alloy and CP-Ti.
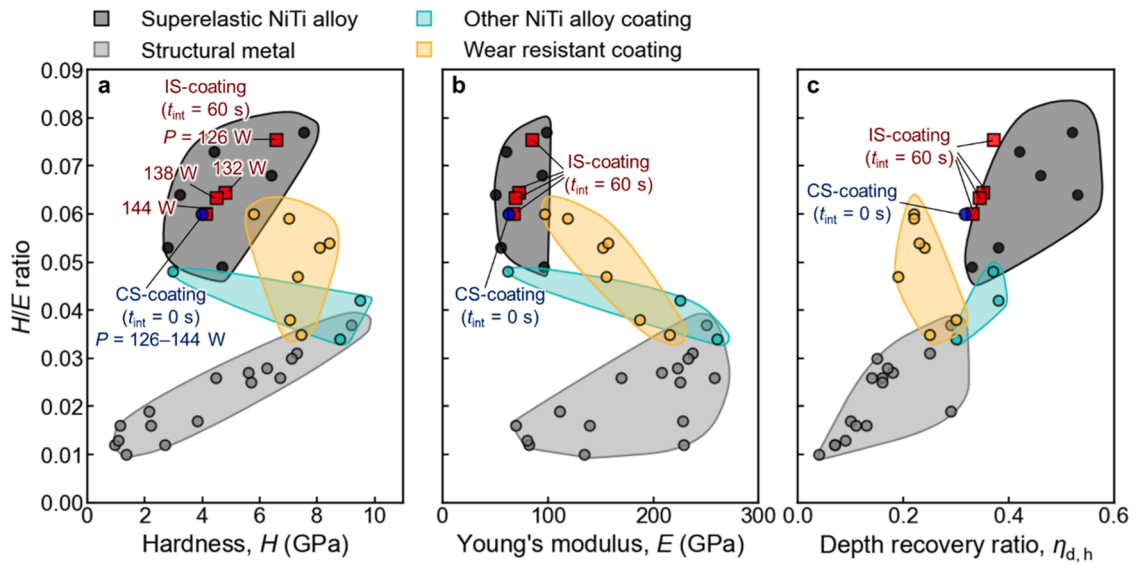
Fig. 9. Comparison of the indentation properties among the IS-coating/CS-coating in the present study, superelastic NiTi alloy [29,56,62,64], structural metal [29, 56,64,69–76], other NiTi alloy coating [67,68], and wear-resistant coating [77–80]. Plot of H/E ratio vs. (a) hardness (H), (b) Young's modulus (E), and (c) depth recovery ratio ($\eta_{d,h}$).

at 126 W shows an H/E ratio higher than that of most SE-NiTi alloys. The EB-scanned coatings exhibit a considerably higher H/E ratio than those of NiTi-coatings fabricated by magnetron sputtering in other studies [67, 68]. This is due to their significantly lower E, despite having H values within the same range.

Fig. 9c compares the $\eta_{d,h}$ of each material. The results show that the $\eta_{d,h}$ of SE-NiTi is considerably higher than that of SM and WR-coatings. This difference arises from the superelastic properties of SE metals, which enable a high reversible strain limit exceeding the elastic strain limit of conventional metals [27,28], leading to significantly higher $\eta_{d,h}$ values. In our study, the $\eta_{d,h}$ of the EB-scanning coatings is higher than that of the SM and WR-coatings and is similar to that of SE-NiTi. In particular, the IS-coating with $P = 126$ W shows the highest $\eta_{d,h}$ in EB-scanned coatings, although it is slightly lower than the average value for SE-NiTi. Similarly, the $\eta_{d,h}$ values reported for NiTi-coatings in other studies [67,68] fall within a comparable range. Although the IS-coatings are mainly composed of the superelastic $B2$-NiTi phase, similar to SE-NiTi, their $\eta_{d,h}$ is reduced due to a higher level of defects compared to that in bulk SE-NiTi and the presence of the $NiTi_2$ phase.

3.5. Frictional wear properties

3.5.1. Sliding wear test results

To further evaluate the wear resistance of the intermittently scanned (IS) coating for practical applications, we conducted friction and wear tests. Fig. 10a presents the friction coefficient curves of IS-coating at 126 and 138 W, comparing them with those of NiTi alloy (SE-NiTi) and CP-Ti. The friction coefficients of the two IS-coatings and SE-NiTi are similar. These coefficients drop sharply to approximately 0.6 within the initial 500–1000 mm of sliding, then fluctuate between 0.5 and 0.7 throughout the remaining sliding distance, showing no indication of stabilization by the end of the test. In contrast, CP-Ti shows the lowest coefficient of friction during the test. It decreases during the initial 2000 mm of sliding, then gradually increases over the sliding distance from 2000 mm to 10,000 mm, stabilizing to around 0.5. The friction coefficients of NiTi coatings are higher than those of CP-Ti, possibly due to the much lower elastic modulus. This lower modulus leads to a larger contact area between the indenter and the NiTi coating during abrasion testing [81], resulting in increased friction. In contrast, the NiTi coating has a similar composition, elastic modulus, and phase structure to
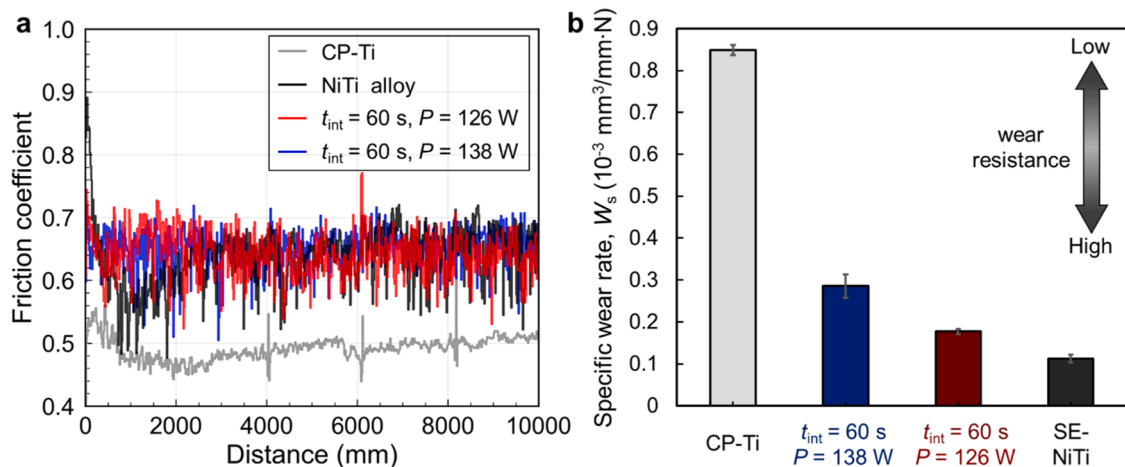
Fig. 10. (a) Friction coefficient curves of two intermittently scanned (IS) coatings, CP-Ti, and NiTi alloy during the sliding wear test. (b) Comparison of specific wear rate (W_s) of IS-coating with CP-Ti and superelastic (SE) NiTi alloy.

SE-NiTi, leading to comparable friction coefficients.

Fig. 10b compares the specific wear rates (W_s) of the two IS-coatings, SE-NiTi, and CP-Ti. The IS-coating produced at 138 W, despite having a higher friction coefficient, exhibits a W_s considerably lower than that of the CP-Ti substrate—approximately 33% W_s of CP-Ti. The IS-coating at 126 W shows a further reduction in W_s, reaching only 20% W_s of CP-Ti. These results confirm that EB-scanned coatings significantly enhance the wear resistance. Elemental and phase composition analyses show that the IS-coating fabricated at 126 W contains a higher concentration of C_{Ni}, more Ni_3Ti phases, and fewer $NiTi_2$ phases compared to the coating produced at 138 W. The high hardness of Ni_3Ti enhances the mechanical strength of the coating [59], while the reduced presence of $NiTi_2$ phases minimizes damage from localized stress concentrations[60], thereby improving wear resistance. These wear test results are aligning with the predictions based on the $\eta_{d,h}$ and H/E ratio data presented in *Section 3.4*.

Additionally, the W_s of the IS-coating at 126 W remains slightly higher than those of SE-NiTi, despite the similarity in elemental composition. The IS-coating at 126 W still contains a small amount of the $NiTi_2$ phase due to compositional inhomogeneity (Figs. 5 and 6), although its primary phase is $B2$-NiTi phase. The $NiTi_2$ phase shows significantly lower hardness and strength than those of the $B2$-NiTi and Ni_3Ti phases and is prone to brittle fracture [59,60]. The presence of the $NiTi_2$ phase is assumed to reduce the overall wear resistance of the IS-coating.

Fig. 11 shows the secondary electron (SE) images and corresponding EDS mapping of the worn surfaces of CP-Ti, IS-coating at 126 W, and superelastic NiTi alloy. The SE images reveal a common phenomenon of scratching and plate-like particle adhesion on the worn surfaces of the three materials. However, the origin of the particles are completely different. EDS mapping of the CP-Ti surface shows only Ti element, indicating that the plate-like particles result from delaminated CP-Ti rather than adhered substances. This suggests that the wear of CP-Ti is caused by both abrasive wear and delamination. The surface delamination of CP-Ti during sliding friction is caused by severe plastic deformation, which induces crack nucleation and propagation parallel to the surface, ultimately leading to delamination [82]. This mechanism contributes to the high W_s and poor wear resistance of CP-Ti.

In contrast, EDS mapping of the EB-scanned coating reveals particles rich in Al, indicating alumina particles detached from the indenter. The NiTi alloy exhibits a similar pattern, with adhered alumina particles

observed on its worn surface. Therefore, the EB-scanned coatings and NiTi alloy do not exhibit delamination under indenter compression. This indicates that the wear of the EB-scanned coatings and NiTi alloys is caused by abrasive wear. In addition, adhesive wear [83] occurring on the alumina indenter side leads to the transfer of alumina debris particles from the indenter, explaining their higher friction coefficients but significantly lower W_s.

3.5.2. Correlation between indentation properties and frictional wear properties

In Fig. 12a, W_s of IS-coating, SE-NiTi, and CP-Ti show a weak negative correlation with H. Hardness, a key result of indentation testing, is often considered a reference indicator of a material's wear resistance. As discussed in *Section 3.4.1*, higher hardness is generally assumed to correspond to better wear resistance, meaning a lower wear rate under identical conditions. However, the results of this study challenge this assumption. SE-NiTi has the lowest W_s among the four materials, yet it does not have the highest H. Figs. 12b and 12c reveal a clearer linear negative correlation between W_s and both the H/E ratio and $\eta_{d,h}$. These results are consistent with the discussion in *Section 3.4.1* that the H/E ratio and $\eta_{d,h}$ are more reliable indicators of wear resistance than H alone.

According to the classical wear theory, one significant cause of wear is localized fracture due to severe plastic deformation of the material surface [83]. Therefore, minimizing plastic deformation is crucial for reducing wear. The relationship between H/E and $\eta_{d,h}$, and the deformation behavior of the material in surface contact provide the mechanism by which these two factors can serve as indicators of wear resistance.

Greenwood and Williamson [84] introduced a "plasticity index" (ψ) for rough contact. In this research, it was concluded that the contact surface deforms plastically under even minimal loads when $\psi > 1$, whereas it deforms predominantly elastically when $\psi < 0.6$. The value of ψ is determined by multiplying E_r/H with geometric factors:

$$\psi = \frac{E_r}{H}\sqrt{\frac{\sigma}{\beta}}. \tag{5}$$

Here, E_r is a reduced modulus, and σ and β are geometric factors dependent only on the contact surface morphology. E_r is defined based
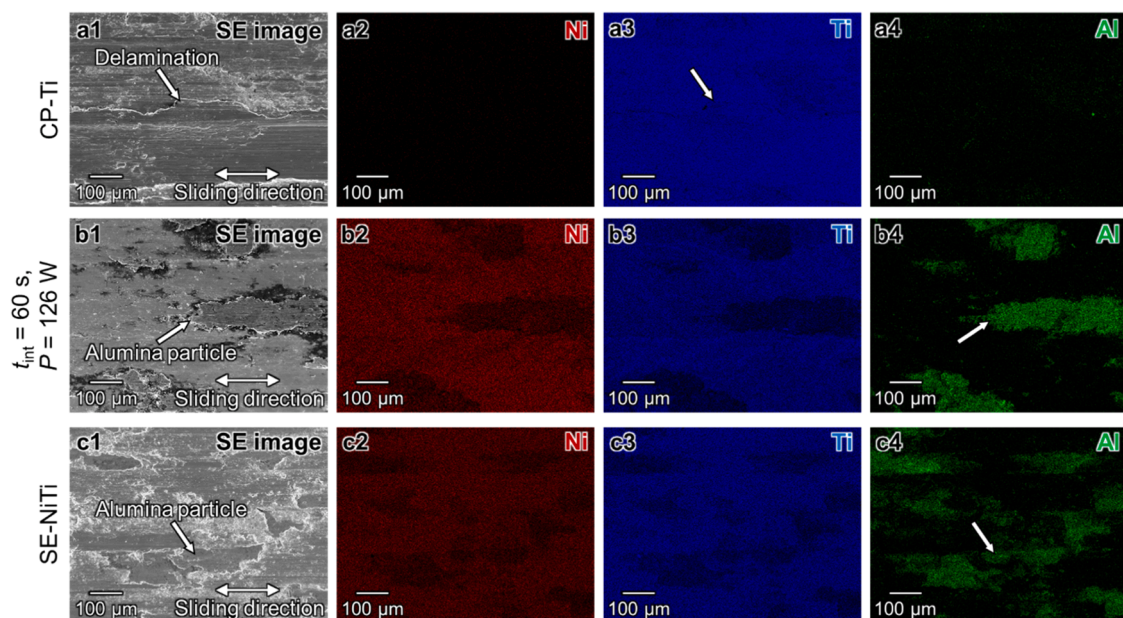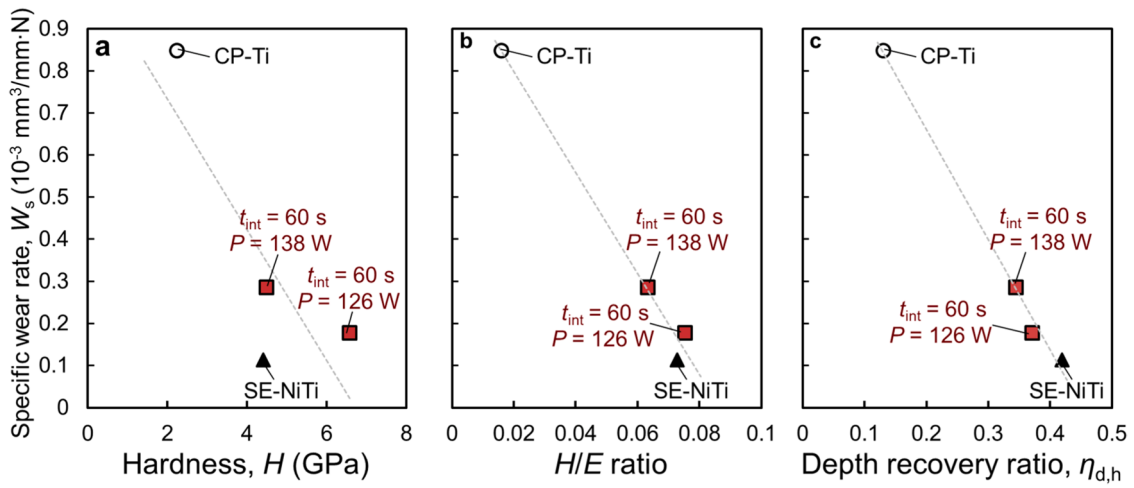

Fig. 11. SE images and EDS elemental mapping of the worn surface on (a) CP-Ti substrate, (b) IS-coating (t_{int} = 60 s, P = 126 W), and (c) superelastic NiTi alloy (SE-NiTi).

Fig. 12. Plot of specific wear rate (W_s) versus (a) Hardness (H), (b) H/E ratio and (c) Depth recovery ratio ($\eta_{d,h}$) among EB-scanned coatings, superelastic NiTi alloy (SE-NiTi), and CP-Ti.

on the modulus (E) and Poisson's ratio (ν) of the specimen, along with the modulus (E_i) and Poisson's ratio (ν_i) of the indenter, as follows:

$$\frac{1}{E_r} = \frac{(1 - \nu^2)}{E} + \frac{(1 - \nu_i^2)}{E_i}. \tag{6}$$

The value of E_r is primarily determined by E when contact occurs between a specimen and a rigid indenter with a large E_i, as is commonly the case in indentation tests and friction wear tests. This indicates that under constant load and contact surface morphology, a larger H/E ratio results in a smaller ψ, which favors elastic deformation. Y.T. Cheng and C.M. Cheng [85–87] investigated in detail the numerical relationships between work, indenter displacement, and material properties such as H and E_r in indentation experiments. From their findings, the following two scaling relationships can be summarized:

$$\frac{W_e}{W_{tot}} \propto \frac{H}{E_r} \tag{7}$$

and

$$\frac{W_e}{W_{tot}} \propto \frac{h_{max} - h_p}{h_{max}} = \eta_{d,h}. \tag{8}$$

Here, W_e is the reversible work, representing the work done by the specimen on the indenter during unloading, and W_{tot} is the total work, representing the work done by the indenter on the specimen during loading. W_e corresponds to the elastic deformation work, while the difference between W_{tot} and W_e represents the irreversible work consumed in plastic deformation. A larger H/E_r or $\eta_{d,h}$ indicates a higher proportion of reversible work to total work, meaning a greater proportion of elastic to total deformation.

These studies suggest that under constant contact conditions, a material with a higher H/E or $\eta_{d,h}$ experiences less plastic deformation and consumes less deformation energy. Thus, it undergoes less surface wear in the friction wear test, resulting in improved wear resistance. The EB-scanned coatings fabricated in this study not only have considerably higher hardness than the CP-Ti substrate, but also very high H/E and $\eta_{d,h}$ comparable to SE-NiTi. Therefore, the EB-scanned coatings achieve low W_s, i.e., excellent wear resistance.

4. Conclusion

A novel fabrication method for NiTi-alloy coating on CP-Ti has been developed utilizing Ni electro-plating and multi-track EB scanning for AM. Four levels of electron beam power (126 W, 132 W, 138 W, and 144 W) were tested in each of the two scanning modes, continuous scanning and intermittent scanning, in order to evaluate the effects of processing parameters on the coating morphology, microstructure, composition, indentation properties, and frictional wear properties. The key findings and conclusions are summarized as follows:

- Implementing an intermittent scanning instead of a continuous scanning strategy can produce coatings with reduced surface roughness.
- Intermittently scanned (IS) coatings exhibit improved composition and microstructure compared to continuously scanned (CS) coatings. In particular, the IS coating fabricated at 126 W shows a Ni concentration exceeding 50 at.%, with a microstructure primarily composed of the superelastic B2-NiTi phase and reinforced by the Ni_3Ti phase.
- All EB-scanned coatings exhibit improved indentation properties compared to uncoated CP-Ti. Among them, the IS-coatings outperform the CS-coatings, showing higher hardness-to-elastic modulus (H/E) ratios and greater depth recovery rates. The IS-coating fabricated at 126 W demonstrates the highest H/E ratio, even higher than that of the superelastic NiTi alloy.
- The IS-coatings fabricated at a power of 126 W demonstrate the most enhanced wear resistance compared to uncoated CP-Ti and other EB scanned coatings, approaching closely those of the superelastic NiTi alloy.
- The EB-scanned NiTi coatings developed in this study—particularly the IS-coating fabricated at 126 W—exhibited the best overall performance. This coating shows potential for use as a wear- or erosion-resistant layer in medical implants and aerospace components.
- Future work will focus on optimizing scanning strategies and processing parameters to eliminate defects in existing coatings and further enhance their performance.

Declaration of generative AI in scientific writing

The authors did not use a generative AI in the writing of this paper.

CRediT authorship contribution statement

Lei Wang: Writing – original draft, Investigation, Funding acquisition, Formal analysis. **Masayuki Okugawa:** Writing – review & editing, Writing – original draft, Methodology, Conceptualization. **Yuheng Liu:** Writing – review & editing, Investigation. **Ken Cho:** Writing – review & editing, Resources, Methodology. **Hiroyuki Y. Yasuda:** Writing – review & editing, Resources, Methodology. **Takayoshi Nakano:** Writing –

review & editing, Resources, Project administration, Methodology, Funding acquisition. **Yuichiro Koizumi:** Writing – review & editing, Supervision, Project administration, Funding acquisition, Conceptualization.

Declaration of competing interest

The authors declare that they have no known competing financial interests or personal relationships that could have appeared to influence the work reported in this paper.

Acknowledgments

Supplementary materials

Supplementary material associated with this article can be found, in the online version, at doi:10.1016/j.surfin.2025.107024.

Data availability

Data will be made available on request.

References

[1] F.A. Shah, M. Trobos, P. Thomsen, A. Palmquist, Commercially pure titanium (cp-Ti) versus titanium alloy (Ti6Al4V) materials as bone anchored implants — Is one truly better than the other? Mater. Sci. Eng. C 62 (2016) 960–966, https://doi.org/10.1016/j.msec.2016.01.032.

[2] R.R. Boyer, An overview on the use of titanium in the aerospace industry, Mater. Sci. Eng. -Struct. Mater. Prop. Microstruct. Process. 213 (1996) 103–114, https://doi.org/10.1016/0921-5093(96)10233-1.

[3] J.R.P. Jorge, V.A. Barão, J.A. Delben, L.P. Faverani, T.P. Queiroz, W.G. Assunção, Titanium in dentistry: historical development, state of the art and future perspectives, J. Indian Prosthodont. Soc. 13 (2013) 71–77, https://doi.org/10.1007/s13191-012-0190-1.

[4] I.V. Gorynin, Titanium alloys for marine application, Mater. Sci. Eng. -Struct. Mater. Prop. Microstruct. Process. 263 (1999) 112–116, https://doi.org/10.1016/S0921-5093(98)01180-0.

[5] A. Kumar, M.K. Mahto, V.S. Rana, M. Vashista, M.Z.K. Yusufzai, Investigation of microstructure evolution and mechanical properties of gas tungsten arc welded dissimilar titanium (CP-Ti/Ti–6Al–4V) alloys, Proc. Inst. Mech. Eng. Part E J. Process Mech. Eng. (2022) 09544089221126431, https://doi.org/10.1177/09544089221126431.

[6] G. Welsch, R. Boyer, E.W. Collings, Materials Properties Handbook: Titanium Alloys, ASM International, 1993.

[7] Y. Qin, L. Geng, D. Ni, Dry sliding wear behavior of extruded titanium matrix composite reinforced by in situ TiB whisker and TiC particle, J. Mater. Sci. 46 (2011) 4980–4985, https://doi.org/10.1007/s10853-011-5415-x.

[8] H. Attar, K.G. Prashanth, A.K. Chaubey, M. Calin, L.C. Zhang, S. Scudino, J. Eckert, Comparison of wear properties of commercially pure titanium prepared by selective laser melting and casting processes, Mater. Lett. 142 (2015) 38–41, https://doi.org/10.1016/j.matlet.2014.11.156.

[9] P. La, J. Ma, Y.T. Zhu, J. Yang, W. Liu, Q. Xue, R.Z. Valiev, Dry-sliding tribological properties of ultrafine-grained Ti prepared by severe plastic deformation, Acta Mater 53 (2005) 5167–5173, https://doi.org/10.1016/j.actamat.2005.07.031.

[10] G. Straffelini, A. Molinari, Mild Sliding Wear of Fe–0.2 %C, Ti–6 %Al–4 %V and Al-7072: a comparative study, Tribol. Lett. 41 (2011) 227–238, https://doi.org/10.1007/s11249-010-9705-2.

[11] Y. Harada, Y. Ishida, D. Miura, S. Watanabe, H. Aoki, T. Miyasaka, A. Shinya, Mechanical properties of selective laser sintering pure titanium and Ti-6Al-4V, and its anisotropy, Materials (Basel) 13 (2020) 5081, https://doi.org/10.3390/ma13225081.

[12] M. Mozetič, Surface Modification to Improve Properties of Materials, Materials (Basel) 12 (2019) 441, https://doi.org/10.3390/ma12030441.

[13] M.S. Safavi, J. Khalil-Allafi, L. Visai, Improved osteogenic activity of NiTi orthopedic implant by HAp-Nb2O5 composite coatings: materials and biological points of view, Biomater. Adv. 150 (2023) 213435, https://doi.org/10.1016/j.bioadv.2023.213435.

[14] M.S. Safavi, A. Rasooli, The positive contribution of Cr2O3 reinforcing nanoparticles to enhanced corrosion and tribomechanical performance of Ni–Mo alloy layers electrodeposited from a citrate-sulfate bath, J. Mater. Res. Technol. 28 (2024) 865–878, https://doi.org/10.1016/j.jmrt.2023.12.014.

[15] H. Bai, L. Zhong, L. Kang, J. Liu, W. Zhuang, Z. Lv, Y. Xu, A review on wear-resistant coating with high hardness and high toughness on the surface of titanium alloy, J. Alloys Compd. 882 (2021) 160645, https://doi.org/10.1016/j.jallcom.2021.160645.

[16] H.E. Rebenne, D.G. Bhat, Review of CVD TiN coatings for wear-resistant applications: deposition processes, properties and performance, Surf. Coat. Technol. 63 (1994) 1–13, https://doi.org/10.1016/S0257-8972(05)80002-7.

[17] H. Cicek, I. Efeoglu, Y. Totik, K.V. Ezirmik, E. Arslan, A low temperature in-situ crystalline TiNi shape memory thin film deposited by magnetron sputtering, Surf. Coat. Technol. 284 (2015) 90–93, https://doi.org/10.1016/j.surfcoat.2015.08.068.

[18] Y. Fu, H. Du, S. Zhang, Adhesion and interfacial structure of magnetron sputtered TiNi films on Si/SiO2 substrate, Thin Solid Films 444 (2003) 85–90, https://doi.org/10.1016/S0040-6090(03)01029-0.

[19] H. Hiraga, T. Inoue, H. Shimura, A. Matsunawa, Cavitation erosion mechanism of NiTi coatings made by laser plasma hybrid spraying, Wear 231 (1999) 272–278, https://doi.org/10.1016/S0043-1648(99)00133-7.

[20] B. Swain, S. Mantry, S.S. Mohapatra, S.C. Mishra, A. Behera, Investigation of tribological behavior of plasma sprayed NiTi coating for aerospace application, J. Therm. Spray Technol. 31 (2022) 2342–2369, https://doi.org/10.1007/s11666-022-01452-7.

[21] A.P. Jardine, Y. Field, H. Herman, Shape memory effect in vacuum plasma sprayed NiTi, J. Mater. Sci. Lett. 10 (1991) 943–945, https://doi.org/10.1007/BF00722140.

[22] M. Bram, A. Ahmad-Khanlou, H.P. Buchkremer, D. Stöver, Vacuum plasma spraying of NiTi protection layers, Mater. Lett. 57 (2002) 647–651, https://doi.org/10.1016/S0167-577X(02)00847-9.

[23] N. Cinca, A. Isalgué, J. Fernández, J.M. Guilemany, Structure characterization and wear performance of NiTi thermal sprayed coatings, Smart Mater. Struct. 19 (2010) 085011, https://doi.org/10.1088/0964-1726/19/8/085011.

[24] S. Tria, O. Elkedim, W.Y. Li, H. Liao, Ball milled Ni–Ti powder deposited by cold spraying, J. Alloys Compd. 483 (2009) 334–336, https://doi.org/10.1016/j.jallcom.2008.08.092.

[25] S. Tria, O. Elkedim, R. Hamzaoui, X. Guo, F. Bernard, N. Millot, O. Rapaud, Deposition and characterization of cold sprayed nanocrystalline NiTi, Powder Technol 210 (2011) 181–188, https://doi.org/10.1016/j.powtec.2011.02.026.

[26] G. Mauer, K.-H. Rauwald, Y.J. Sohn, T.E. Weirich, Cold gas spraying of nickel-titanium coatings for protection against cavitation, J. Therm. Spray Technol. 30 (2021) 131–144, https://doi.org/10.1007/s11666-020-01139-x.

[27] H. Tobushi, K. Tanaka, T. Hori, T. Sawada, T. Hattori, Pseudoelasticity of TiNi shape memory alloy : dependence on maximum strain and temperature, JSME Int. J. Ser Mech. Mater. Eng. 36 (1993) 314–318, https://doi.org/10.1299/jsmea1993.36.3_314.

[28] L. Hou, D.S. Grummon, Transformational superelasticity in sputtered titanium-nickel thin films, Scr. Metall. Mater. 33 (1995) 989–995, https://doi.org/10.1016/0956-716X(95)00311-I.

[29] C. Zhang, Z.N. Farhat, Sliding wear of superelastic TiNi alloy, Wear 267 (2009) 394–400, https://doi.org/10.1016/j.wear.2008.12.093.

[30] W. Ni, Y.-T. Cheng, D.S. Grummon, Recovery of microindents in a nickel–titanium shape-memory alloy: a "self-healing" effect, Appl. Phys. Lett. 80 (2002) 3310–3312, https://doi.org/10.1063/1.1476064.

[31] R. Liu, D.Y. Li, Y.S. Xie, R. Llewellyn, H.M. Hawthorne, Indentation behavior of pseudoelastic TiNi alloy, Scr. Mater. 41 (1999) 691–696, https://doi.org/10.1016/S1359-6462(99)00199-2.

[32] M.Mansoob Khan, 11 - Electrochemical deposition synthesis methods, in: M. Mansoob Khan (Ed.), Photocatal. Synth. Charact. Methods, Elsevier, 2025, pp. 113–123, https://doi.org/10.1016/B978-0-443-28913-2.00012-5.

[33] M.S. Safavi, J. Khalil-Allafi, A. Motallebzadeh, C. Volpini, V. Khalili, L. Visai, Encouraging tribomechanical and biological responses of hydroxyapatite coatings reinforced by various levels of niobium pentoxide particles, Mater. Adv. 4 (2023) 5618–5632, https://doi.org/10.1039/D3MA00704A.

[34] M.S. Safavi, S. Soleimanzadeh Ghazijahani, A. Rasooli, Pulsed electroplating of ZrO2-reinforced Ni-Cr alloy coatings from the duplex complexing agents-containing bath for engineering applications: importance of operating conditions, Heliyon 10 (2024) e37631, https://doi.org/10.1016/j.heliyon.2024.e37631.

[35] K. Turalıoğlu, M. Taftalı, H. Tekdir, O. Çomaklı, M. Yazıcı, T. Yetim, A.F. Yetim, The tribological and corrosion properties of anodized Ti6Al4V/316L bimetallic structures manufactured by additive manufacturing, Surf. Coat. Technol. 405 (2021) 126635, https://doi.org/10.1016/j.surfcoat.2020.126635.

[36] H. Tekdir, T. Yetim, A.F. Yetim, Corrosion Properties of Ceramic-Based TiO2 Films on Plasma Oxidized Ti6Al4V/316L Layered Implant Structured Manufactured by Selective Laser Melting, J. Bionic Eng. 18 (2021) 944–957, https://doi.org/10.1007/s42235-021-0055-6.

[37] H. Tekdir, A.F. Yetim, Additive manufacturing of multiple layered materials (Ti6Al4V/316L) and improving their tribological properties with glow discharge surface modification, Vacuum 184 (2021) 109893, https://doi.org/10.1016/j.vacuum.2020.109893.

[38] L. Wang, M. Okugawa, H. Konishi, Y. Liu, Y. Koizumi, T. Nakano, Fusion of Ni plating on CP-titanium by electron beam single-track scanning: toward a new approach for fabricating TiNi self-healing shape memory coating, Materials (Basel) 16 (2023) 5449, https://doi.org/10.3390/ma16155449.

[39] Y. Huang, M.B. Khamesee, E. Toyserkani, A new physics-based model for laser directed energy deposition (powder-fed additive manufacturing): from single-track

to multi-track and multi-layer, Opt. Laser Technol. 109 (2019) 584–599, https://doi.org/10.1016/j.optlastec.2018.08.015.

[40] Denki Kagaku Kai (Ed.), Denki Kagaku Benran [Electrochemical Handbook], 6th ed., Maruzen Publishing, Tōkyō, 2013 in Japanese.

[41] Thermo-Calc Software, Titanium and TiAl-based Alloys Databases, Version 4 (TCTI4). https://thermocalc.com/products/databases/, 2022 accessed October 1, 2023.

[42] E.S. Berkovich, The three-faceted diamond pyramid for microhardness testing, Ind. Diamond Rev. 11 (127) (1951) 129–133.

[43] A. Shimamoto, K. Tanaka, Y. Akiyma, H. Yoshizaki, Nanoindentation of glass with a tip-truncated Berkovich indenter, Philos. Mag. A 74 (1996) 1097–1105, https://doi.org/10.1080/01418619608239710.

[44] International Organization for Standardization, Metallic materials — Instrumented indentation test for hardness and materials parameters — Part 1: test method (ISO Standard No. 14577-1:2015). https://www.iso.org/standard/56626.html, 2015.

[45] W. Ni, Y.-T. Cheng, D.S. Grummon, Microscopic superelastic behavior of a nickel-titanium alloy under complex loading conditions, Appl. Phys. Lett. 82 (2003) 2811–2813, https://doi.org/10.1063/1.1569984.

[46] ASTM International, Test Method for Linearly Reciprocating Ball-on-Flat Sliding Wear, (2022). https://doi.org/10.1520/G0133-22.

[47] J.F. Shackelford, W. Alexander (Eds.), CRC Materials Science and Engineering Handbook, 3rd ed., CRC Press, Boca Raton, 2000 https://doi.org/10.1201/9781420038408.

[48] S.K. Ray, A. Banerjee, B.K. Bhangi, D. Pyne, B. Dutta, 2 - Tribological analysis—General test standards, in: S.C. George, J.T. Haponiuk, S. Thomas, R. Reghunath, S.P. s (Eds.), Tribol. Polym. Polym. Compos. Polym. Nanocomposites, Elsevier, 2023, pp. 17–50, https://doi.org/10.1016/B978-0-323-90748-4.00001-7.

[49] C. Li, Z.Y. Liu, X.Y. Fang, Y.B. Guo, Residual Stress in Metal Additive Manufacturing, Procedia CIRP 71 (2018) 348–353, https://doi.org/10.1016/j.procir.2018.05.039.

[50] A. Takase, T. Ishimoto, R. Suganuma, T. Nakano, Surface residual stress and phase stability in unstable β-type Ti–15Mo–5Zr–3Al alloy manufactured by laser and electron beam powder bed fusion technologies, Addit. Manuf. 47 (2021) 102257, https://doi.org/10.1016/j.addma.2021.102257.

[51] Y. Miyata, M. Okugawa, Y. Koizumi, T. Nakano, Inverse Columnar-Equiaxed Transition (CET) in 304 and 316L Stainless Steels Melt by Electron Beam for Additive Manufacturing (AM), Crystals 11 (2021) 856, https://doi.org/10.3390/cryst11080856.

[52] L.E. Criales, Y.M. Arısoy, B. Lane, S. Moylan, A. Donmez, T. Özel, Predictive modeling and optimization of multi-track processing for laser powder bed fusion of nickel alloy 625, Addit. Manuf. 13 (2017) 14–36, https://doi.org/10.1016/j.addma.2016.11.004.

[53] Y. Cheng, G. Wang, Z. Qiu, Z. Zheng, D. Zeng, X. Tang, R. Shi, M. Uddagiri, I. Steinbach, Multi-physics simulation of non-equilibrium solidification in Ti-Nb alloy during selective laser melting, Acta Mater 272 (2024) 119923, https://doi.org/10.1016/j.actamat.2024.119923.

[54] S. Katayama, 12 - Defect formation mechanisms and preventive procedures in laser welding, in: S. Katayama (Ed.), Handb. Laser Weld. Technol, Woodhead Publishing, 2013, pp. 332–373, https://doi.org/10.1533/9780857098771.2.332.

[55] G. Baigonakova, E. Marchenko, T. Chekalkin, J. Kang, S. Weiss, A. Obrosov, Influence of Silver Addition on Structure, Martensite Transformations and Mechanical Properties of TiNi–Ag Alloy Wires for Biomedical Application, Materials (Basel) 13 (2020) 4721, https://doi.org/10.3390/ma13214721.

[56] Z.N. Farhat, C. Zhang, The role of reversible martensitic transformation in the wear process of TiNi shape memory alloy, Tribol. Trans. 53 (2010) 917–926, https://doi.org/10.1080/10402004.2010.510620.

[57] Z. Pang, Q. Zeng, Z. Ning, W. He, Z. Wang, J. Wang, L. Li, Ultralow friction and low wear behavior of in-situ formed NiTiO3 from 60NiTi alloy at 350 °C, Intermetallics 168 (2024) 108271, https://doi.org/10.1016/j.intermet.2024.108271.

[58] K. Otsuka, K. Shimizu, Pseudoelasticity and shape memory effects in alloys, Int. Met. Rev. 31 (1986) 93–114, https://doi.org/10.1179/imtr.1986.31.1.93.

[59] Z. Liu, L. Zhang, C. Fu, C. Zeng, X. Wu, W. Li, X. Ma, Structural, mechanical, and thermodynamic properties of Ni–Ti intermetallic compounds: first-principle calculation, J. Appl. Phys. 134 (2023) 085107, https://doi.org/10.1063/5.0159431.

[60] Y. Tian, Z. Liang, Y. Cai, H. Jiang, M. Chen, J. Han, Microstructure and mechanical properties of Ti2Ni alloy fabricated by direct energy deposition, Sci. Technol. Weld. Join. 29 (2024) 47–51, https://doi.org/10.1177/13621718231216674.

[61] L. Yang, M. Wen, X. Dai, G. Cheng, K. Zhang, Ultrafine Ceramic Grains Embedded in Metallic Glass Matrix: achieving Superior Wear Resistance via Increase in Both Hardness and Toughness, ACS Appl. Mater. Interfaces 10 (2018) 16124–16132, https://doi.org/10.1021/acsami.8b02338.

[62] R. Neupane, Z. Farhat, Wear Resistance and Indentation Behavior of Equiatomic Superelastic TiNi and 60NiTi, Mater. Sci. Appl. 6 (2015) 694–706, https://doi.org/10.4236/msa.2015.67071.

[63] R.C.D. Richardson, The wear of metals by relatively soft abrasives, Wear 11 (1968) 245–275, https://doi.org/10.1016/0043-1648(68)90175-0.

[64] W. Ni, Y.-T. Cheng, M. Lukitsch, A.M. Weiner, L.C. Lev, D.S. Grummon, Novel layered tribological coatings using a superelastic NiTi interlayer, Wear 259 (2005) 842–848, https://doi.org/10.1016/j.wear.2005.01.015.

[65] A. Leyland, A. Matthews, On the significance of the H/E ratio in wear control: a nanocomposite coating approach to optimised tribological behaviour, Wear 246 (2000) 1–11, https://doi.org/10.1016/S0043-1648(00)00488-9.

[66] B.D. Beake, The influence of the H/E ratio on wear resistance of coating systems – Insights from small-scale testing, Surf. Coat. Technol. 442 (2022) 128272, https://doi.org/10.1016/j.surfcoat.2022.128272.

[67] N. Cameron, Z. Farhat, Investigation into the wear and dent resistance of Ni/Ti nanolaminates and superelastic NiTi coating, J. Mater. Eng. Perform. 28 (2019) 6033–6041, https://doi.org/10.1007/s11665-019-04377-5.

[68] K.L. Ng, Q.P. Sun, M. Tomozawa, S. Miyazak, Wear behavior of NiTi thin film at micro-scale, Int. J. Mod. Phys. B 24 (2010) 85–93, https://doi.org/10.1142/S0217979210064010.

[69] H. Vafaeenezhad, S. Aliakbari-Sani, S.H. Seyedein, A. Ghosh, A.R. Eivani, Flow behavior and strain rate sensitivity assessment of γ and γ' phases in Co–Al–W-based superalloy using experimental and computational approaches, J. Mater. Res. Technol. 18 (2022) 4617–4630, https://doi.org/10.1016/j.jmrt.2022.03.166.

[70] W. Xiufang, Y. Xiaoping, G. Zhendan, Z. Yinchang, S. Hongwei, Nanoindentation characterization of mechanical properties of ferrite and austenite in duplex stainless steel, Adv. Mater. Res. 24–25 (2007) 1165–1170, https://doi.org/10.4028/www.scientific.net/AMR.26-28.1165.

[71] Z. Wang, J. Zhang, H.U. Hassan, Z. Zhang, Y. Yan, A. Hartmaier, T. Sun, Coupled effect of crystallographic orientation and indenter geometry on nanoindentation of single crystalline copper, Int. J. Mech. Sci. 148 (2018) 531–539, https://doi.org/10.1016/j.ijmecsci.2018.09.007.

[72] L. Zhu, B. Xu, H. Wang, C. Wang, D. Yang, Measurement of mechanical properties of 1045 steel with significant pile-up by sharp indentation, J. Mater. Sci. 46 (2011) 1083–1086, https://doi.org/10.1007/s10853-010-4876-7.

[73] A. Liu, Q. Pan, M. Chen, W. Xu, W. Chen, An investigation on the relationships between hardness, elas- ticmodulus and the work of 7075 aluminium alloy by nanoindentation, J. Phys. Conf. Ser. 2044 (2021) 012106, https://doi.org/10.1088/1742-6596/2044/1/012106.

[74] X.Y. Li, J.R. Ye, B. Tang, Study of the Ion Nitrided Layer on Ti-6Al-4V substrate, Adv. Mater. Res. 79–82 (2009) 695–698, https://doi.org/10.4028/www.scientific.net/AMR.79-82.695.

[75] M. Liu, Q. Zheng, X. Wang, C. Xu, Characterization of Distribution of Microstructure and Micro-mechanical Properties of Nickel-Based Single Crystal Superalloy Within the Shot-Peened Layer, Met. Mater. Int. 29 (2023) 2257–2286, https://doi.org/10.1007/s12540-023-01388-9.

[76] M. Zhang, F. Li, B. Chen, S. Wang, Investigation of micro-indentation characteristics of P/M nickel-base superalloy FGH96 using dislocation-power theory, Mater. Sci. Eng. A 535 (2012) 170–181, https://doi.org/10.1016/j.msea.2011.12.060.

[77] J. Nohava, B. Bonferroni, G. Bolelli, L. Lusvarghi, Interesting aspects of indentation and scratch methods for characterization of thermally-sprayed coatings, Surf. Coat. Technol. 205 (2010) 1127–1131, https://doi.org/10.1016/j.surfcoat.2010.08.086.

[78] J.G. La Barbera-Sosa, Y.Y. Santana, M.H. Staia, D. Chicot, J. Lesage, J. Caro, G. Mesmacque, E.S. Puchi-Cabrera, Microstructural and mechanical characterization of Ni-base thermal spray coatings deposited by HVOF, Surf. Coat. Technol. 202 (2008) 4552–4559, https://doi.org/10.1016/j.surfcoat.2008.04.041.

[79] C. Leither, J. Risan, M. Bashirzadeh, F. Azarmi, Determination of the elastic modulus of wire arc sprayed alloy 625 using experimental, analytical, and numerical simulations, Surf. Coat. Technol. 235 (2013) 611–619, https://doi.org/10.1016/j.surfcoat.2013.08.033.

[80] P. Poza, C.J. Múnez, M.A. Garrido-Maneiro, S. Vezzù, S. Rech, A. Trentin, Mechanical properties of Inconel 625 cold-sprayed coatings after laser remelting. Depth sensing indentation analysis, Surf. Coat. Technol. 243 (2014) 51–57, https://doi.org/10.1016/j.surfcoat.2012.03.018.

[81] J.A. Greenwood, Analysis of elliptical Hertzian, Tribol. Int. 30 (1997) 235–237, https://doi.org/10.1016/S0301-679X(96)00051-5.

[82] N.P. Suh, The delamination theory of wear, Wear 25 (1973) 111–124, https://doi.org/10.1016/0043-1648(73)90125-7.

[83] K.G. Budinski, Surface Engineering For Wear Resistance, Prentice Hall, Englewood Cliffs, N.J., 1988. http://archive.org/details/surfaceengineeri0000budi. accessed December 30, 2024.

[84] J.A. Greenwood, J.B.P. Williamson, Contact of nominally flat surfaces, Proc. R. Soc. Lond. Ser. Math. Phys. Sci. 295 (1966) 300–319, https://doi.org/10.1098/rspa.1966.0242.

[85] Y.-T. Cheng, C.-M. Cheng, Relationships between hardness, elastic modulus, and the work of indentation, Appl. Phys. Lett. 73 (1998) 614–616, https://doi.org/10.1063/1.121873.

[86] Y.-T. Cheng, Z. Li, C.-M. Cheng, Scaling relationships for indentation measurements, Philos. Mag. A 82 (2002) 1821–1829, https://doi.org/10.1080/01418610208235693.

[87] Y.-T. Cheng, C.-M. Cheng, Scaling, dimensional analysis, and indentation measurements, Mater. Sci. Eng. R Rep. 44 (2004) 91–149, https://doi.org/10.1016/j.mser.2004.05.001.